

# PASSIVE SCALAR STIRRING BY MULTISCALE-GENERATED TURBULENCE

**S. Laizet**

Turbulence, Mixing and Flow Control Group,  
Department of Aeronautics, Imperial College London  
London, SW7 2BY, United Kingdom  
s.laizet@imperial.ac.uk

**J.C. Vassilicos**

Turbulence, Mixing and Flow Control Group,  
Department of Aeronautics, Imperial College London  
London, SW7 2BY, United Kingdom  
j.c.vassilicos@imperial.ac.uk

## ABSTRACT

The stirring and mixing of a passive scalar by fractal generated turbulence in the presence of a mean scalar gradient is studied in three dimensions by DNS (Direct Numerical Simulation). Passive scalar behaviour is of preliminary importance in turbulent mixing and can also provide an opportunity to understand turbulence itself. Recent experiments in wind tunnels [1, 2] have shown that it is possible to tune fractal objects (see figure 1) as very efficient turbulence generators of potential use for static inline mixers. In this numerical work, turbulent mixing in regular and fractal grid turbulence is investigated with a Prandtl number of 0.1. The results show that it is possible to improve turbulent stirring and heat transfer mixing by using a fractal square grid instead of a regular grid, even with the same blockage ratio and the same input velocity.

## Introduction

Recently, [1, 2] used different multiscale grids to generate turbulence in a wind tunnel and have shown that complex multiscale boundary/initial conditions can drastically influence the behaviour of a turbulent flow, especially when a fractal square grid (see figure 1) is placed at the entry of a wind tunnel test section. Fractal geometry is a concept where a given pattern (cross, square or I as in figure 1) is repeated and split into parts, each being a reduced-copy of the whole. Multiscale (fractal) objects can be designed to be immersed in any fluid flow where there is a need to control and design the turbulence generated by the object. The experiments have shown that, unlike regular objects (where the turbulence is generated by only one scale), a slight modification of one of the multiscale object's parameters can deeply modify the turbulence generated by the fluid's impact on the object. Multiscale objects offer the opportunity to discover new complex flow effects/interactions that can help understand how to control and/or manage complex fluid flows. Furthermore, such

multiscale objects can be designed as energy-efficient mixers with high turbulent intensities and a small pressure drop. [3] have shown that fractal grids can be designed as stirring elements for inline static mixers and, as such, that they compare favourably with commercially available state-of-the-art stirring elements.

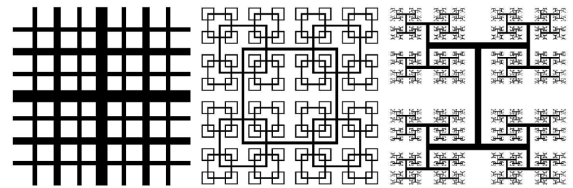


Figure 1. Scaled diagrams of a fractal cross grid (left), a fractal square grid (middle) and a fractal I grid (right).

The organisation of this paper is as follows. In the following section, we present the DNS methodology, a brief description of the grids and the numerical parameters of each simulation. Some visualisations are presented and discussed in section 2. Then, in order to better understand the underlying properties of each flow, some statistical results are presented in the penultimate section, followed by a conclusion in the last section.

## 1 Flow parameters and numerical modelling

### 1.1 Numerical Methods

To solve the incompressible Navier-Stokes equations and the transport equation for the passive scalar, we use a numerical code (called **Incompact3d**) based on sixth-order compact

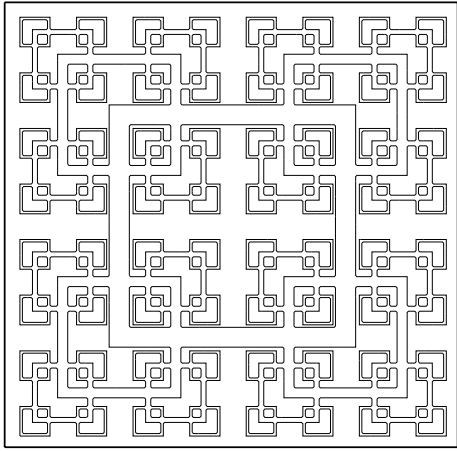
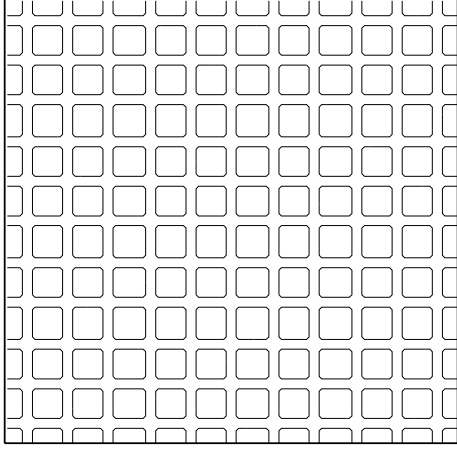


Figure 2. Scaled diagram of the regular grid (top) and the fractal square grid (bottom).

schemes for spatial discretization and a third order Adams-Bashforth scheme for time advancement. To treat the incompressibility condition, a fractional step method requires to solve a Poisson equation. This equation is fully solved in spectral space, via the use of relevant 3D Fast Fourier Transforms. The pressure mesh is staggered from the velocity mesh by half a mesh, to avoid spurious pressure oscillations. With the help of the concept of modified wave number, the divergence free condition is ensured up to machine accuracy. More details about the present code and its validations, especially the original treatment of the pressure in the spectral space, can be found in [4]. The modelling of the grids is performed by an Immersed Boundary Method, following a procedure proposed by [5]. The present method is a direct forcing approach that ensures the no-slip boundary condition at the grid walls. It mimics the effects of a solid surface on the fluid with an extra forcing in the Navier-Stokes equations.

Because of the size of the simulations, the parallel version of **Incompact3d** has been used for this numerical work. Based on a highly scalable 2D decomposition library and a

distributed FFT interface, it is possible to use the code on thousands of computational cores. More details about this efficient parallel strategy can be found in [6].

## 1.2 Governing equations

The governing equations are the forced Navier-Stokes equations and the transport equation for the passive scalar:

$$\frac{\partial \mathbf{u}}{\partial t} = -\nabla p - \frac{1}{2} [\nabla (\mathbf{u} \otimes \mathbf{u}) + (\mathbf{u} \cdot \nabla) \mathbf{u}] + \nu \nabla^2 \mathbf{u} + \mathbf{f} \quad (1)$$

$$\nabla \cdot \mathbf{u} = 0 \quad (2)$$

$$\frac{\partial \theta}{\partial t} + \mathbf{u} \cdot \nabla \theta + S = \frac{1}{Re_{t_{min}} Pr} \nabla^2 \theta \quad (3)$$

where  $p(\mathbf{x}, t)$  is the pressure field (for a fluid with a constant density  $\rho = 1$ ),  $\mathbf{u}$  the velocity field,  $\theta$  the passive scalar field,  $S = \nu S_\theta$  with  $S_\theta = 1/16$  being a constant scalar gradient and  $\nu$  the lateral viscosity, and  $Pr$ , the Prandtl number (equal to 0.1). In this work, the forcing field  $\mathbf{f}(\mathbf{x}, t)$  is used through an immersed boundary method in order to take into account the grid inside the computational domain. Note that the passive scalar configuration, in particular  $S$ , is based on the works of [7, 8].

## 1.3 Numerical Parameters

For the fractal square grid, the computational domain  $L_x \times L_y \times L_z = 1152t_{min} \times 144t_{min} \times 144t_{min}$  is discretized on a Cartesian mesh of  $n_x \times n_y \times n_z = 2881 \times 360 \times 360$  mesh nodes, about 374 million mesh nodes in total. It is split in 8100 computational cores. For the regular grid, the computational domain  $L_x \times L_y \times L_z = 1152t_{min} \times 72t_{min} \times 72t_{min}$  is discretized on a Cartesian mesh of  $n_x \times n_y \times n_z = 2881 \times 180 \times 180$  mesh nodes, about 93 million mesh nodes in total. It is split in 7200 computational cores. Unlike the regular grid, the fractal grid does not have a well-defined mesh size. [1] introduced an effective mesh size  $M_{eff} = \frac{4T^2}{P} \sqrt{1-\sigma}$  where  $P$  is the grid's fractal perimeter's length,  $T$  the lateral size of the wind tunnel and  $\sigma$  the blockage ratio. When applied to a regular grid,  $M_{eff}$  equals the actual mesh size of the grid. For each grid, the simulation is performed with a Reynolds number  $Re_{M_{eff}} = 2000$  (based on the effective mesh size of the two grids  $M_{eff}$  and the streamwise upstream velocity  $U_\infty$ , it corresponds to a velocity of about  $1.5m/s$  in a wind tunnel). The time step  $\Delta t = 0.01t_{min}/U_\infty$  is low enough to have a CFL condition of about 0.75. The streamwise position of the grid ( $14M_{eff}$  from the inflow boundary of the computational domain) has been carefully chosen to avoid any spurious interactions between the modelling of the grid and the inflow boundary condition. Note that the simulations are performed with the same Reynolds number (based on  $M_{eff}$ , equal to 2000, same blockage ratio ( $\sigma = 50.7\%$ ) and same effective mesh size ( $M_{eff} = 6.5t_{min}$ ) for the fractal square grid and the regular grid. In the calculations presented here, boundary conditions are inflow/outflow in the direction  $x$  of the mean flow

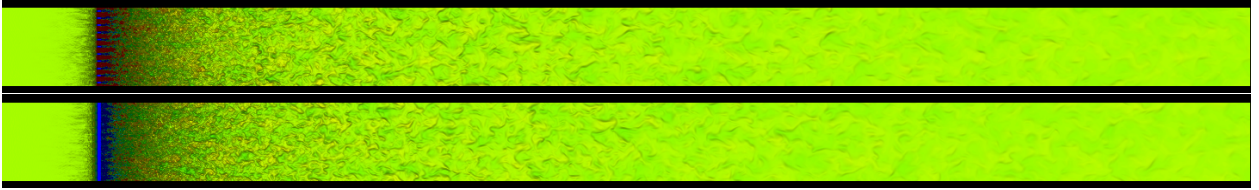


Figure 3. Instantaneous streamwise velocity field obtained for the regular grid in the  $(x - y)$  plane: behind a bar (top) and in the middle between two bars (bottom). Values above  $1.5U_\infty$  are in red while negative values are in blue.

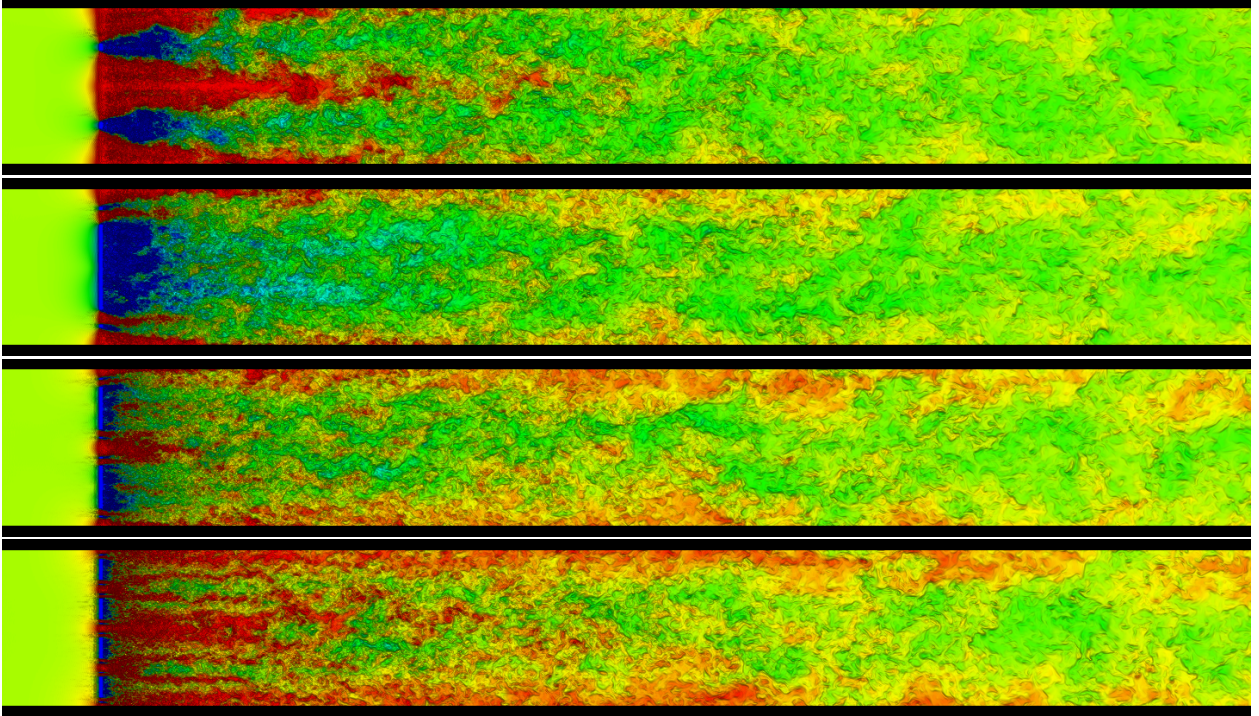


Figure 4. Instantaneous streamwise velocity field obtained for the fractal square grid at different lateral location in the  $(x - y)$  plane. Values above  $1.5U_\infty$  are in red while negative values are in blue.

(velocity boundary conditions of Dirichlet type) and periodic in directions  $y$  and  $z$ . The inflow condition is a uniform profile ( $U_\infty = 1$ ) with no turbulence.

## 2 Results: instantaneous visualisations

Figures 3 and 4 illustrate our two turbulent flows by showing snapshots of instantaneous streamwise velocity fields at different  $(x - y)$  planes. A non-homogeneous turbulent field is obtained close to the grids, but in the case of the regular grid, the turbulence does homogenise relatively close to the grid. Instead, the turbulence remains non-homogeneous for a long distance downstream of the fractal grid. For the fractal square grid, there is a clear presence of wakes of four different sizes, corresponding to the four fractal iterations of the grid. These snapshots suggest that the levels of turbulence generated by the fractal grids seems to be more important than for the regular grid, except very close to the grid. It is important to recall that the two grids have the same blockage ratio and that the same input velocity is used in the two configurations.

Figures 5 and 6 show snapshots of instantaneous passive

scalar fields at different  $(x - y)$  planes. Note that in the two figures the color levels are the same. The passive scalar fluctuations are created by the turbulence generated by the grids and the uniform scalar gradient  $S_\theta$  (no passive scalar fluctuations are imposed at the inlet of the computational domain). As expected, a uniform passive scalar field is obtained behind the regular grid, with relatively small levels of fluctuations. In contrast, we can observe high levels of fluctuations for the passive scalar generated behind the fractal square grid, with much bigger structures in the second half of the computational domain.

## 3 Results: statistics

Figure 7 (top) shows the streamwise evolution of the normalised rms  $(u'^2)^{1/2}/U_\infty$  of the turbulent fluctuations obtained by averaging in time. As expected from previously reported wind tunnel measurements and simulations [1, 9–11], the turbulent flow generated by the fractal grid exhibits two regions on the centreline of the flow: starting immediately after the grid, a protracted production region where the turbu-

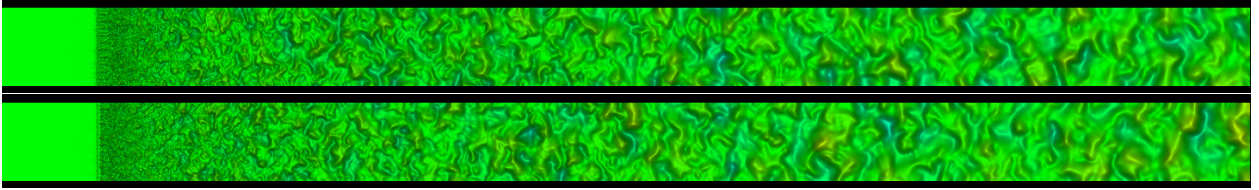


Figure 5. Instantaneous passive scalar field obtained for the regular grid in the  $(x-y)$  plane: behind a bar (top) and in the middle between two bars (bottom). Values above 1.5 are in red while values below  $-1.5$  are in blue.

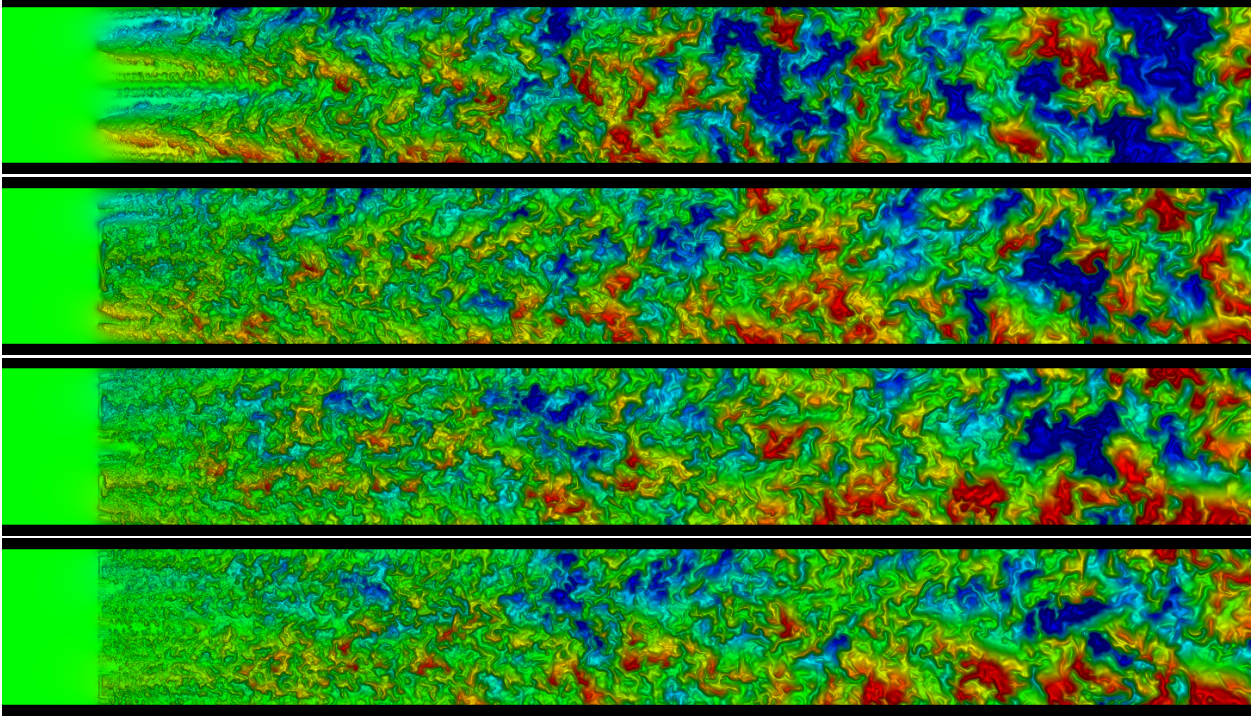


Figure 6. Instantaneous passive scalar field obtained for the fractal square grid at different lateral location in the  $(x-y)$  plane.. Values above 1.5 are in red while values below  $-1.5$  are in blue.

lence continuously intensifies reaching a turbulence intensity peak at a far point where the second region starts and in which the turbulence decays. This has been observed in wind tunnel experiments [1, 9] for low blockage fractal square grids and along various straight lines in the streamwise direction.

Figure 7 (bottom) shows the streamwise evolution of the normalised rms  $(u'^2)^{1/2}/U_\infty$  of the turbulent fluctuations normalised by its peak value as a function of  $x/x_*$ . Introduced by [9],  $x_*$  is defined as

$$x_* = \frac{L_0^2}{t_0} \quad (4)$$

where  $L_0$  is the lateral length of the biggest square and  $t_0$  the lateral thickness of the biggest square of the grid. Note that for the fractal grid,  $L_0 = L_y/2$  and  $t_0 = 8.5t_{min}$  (with  $t_{min} = 1$ ) and for the regular grid,  $L_0 = M_{eff}$  and  $t_0 = 2t_{min}$ . As suggested by [9],  $x_*$  can be seen as a characteristic length scale of interactions between the wake of the largest grid bars. One can clearly see that it is possible to collapse the data for both grids up to  $x/x_* \approx 0.5$ , through not at higher value of  $x/x_*$ .

Another interesting result arises from comparing the streamwise evolutions of the turbulence by doing a spatial average of  $(u'^2)^{1/2}/U_\infty$  in the  $(y-z)$  plane. We found that at the end of the computational domain, we have about 7.5% of turbulence for the fractal grid while we have only about 2.5% for the regular grid.

Figure 8 shows the streamwise profiles along the centreline of the flow of the turbulent Reynolds number  $Re_\lambda = u'\lambda/\nu$  based on the Taylor microscale  $\lambda = u'^2 / \langle (\partial u / \partial x)^2 \rangle$  and the turbulent intensity  $u'$ . The fractal square grid generates a Reynolds number  $Re_\lambda$  more than four times bigger than the regular grid despite the same  $Re_{M_{eff}}$  and the same blockage ratio, in good agreement with the experimental results of [1]. This confirms that the fractal square grids are able to generate much more turbulence than a regular grid [11]. Furthermore, after the peak  $Re_\lambda$  is roughly constant for the regular grid whereas it is decreasing for the fractal square grid.

Figure 9 shows the streamwise profiles of the passive scalar variance and the passive scalar flux along the centreline of the flow in one case and averaged in the  $(y-z)$  plane in the other. One of the main interesting results here is that we can

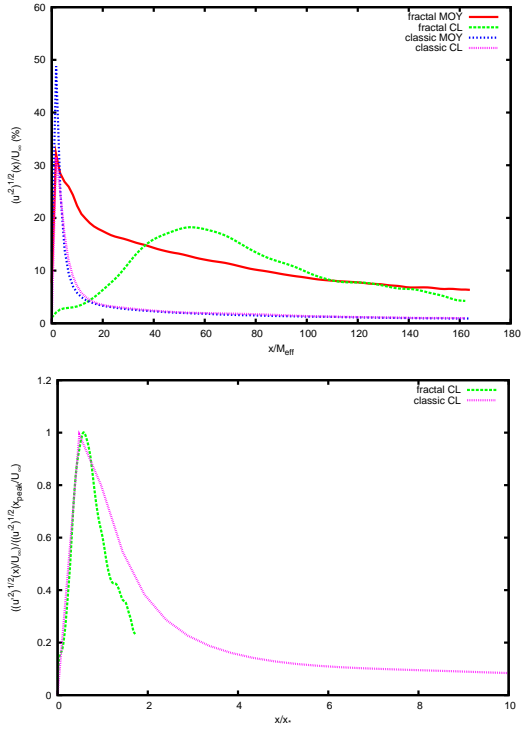


Figure 7. Streamwise evolution of the normalised rms  $(u^2)^{1/2}/U_\infty$  of the turbulent fluctuations (top) normalised by its value at  $x_{peak}$  as a function of  $x/(x_*\sigma)$  (bottom).

observe a continuous increase for the passive scalar variance, much more pronounced for the fractal square grid. At the end of the computational domain, the variance is more than ten times bigger for the fractal grid. One can assume that this is due to the source term  $S_\theta$  which has been greatly enhanced by the fractal-generated turbulence and is much stronger than the passive scalar dissipation. Indeed, [7] predicted that the level of the passive scalar fluctuations would increase indefinitely with streamwise distance if the dissipation is neglected for a similar passive scalar configuration. Furthermore, we notice a linear increase of the passive scalar variance, in agreement with the experiments of [12, 13] where the authors found that the variance should grow linearly with streamwise distance in decaying turbulent grid flow.

Another key result here is that, after  $x/M_{eff} \approx 40$ , the scalar flux is almost constant for both grids. Like for the variance, the flux is more than ten times bigger for the fractal square grid. This significant production of scalar flux, combined with the high level of turbulence, strongly affects the passive scalar variance, and explains why it is very large for the fractal square grid.

#### 4 Conclusion

Two spatially evolving turbulent flows generated by a regular and a fractal square grid have been investigated by means of DNS. In this work we have focused on the properties of stirring of a scalar by a turbulent velocity field in the presence of an imposed mean scalar gradient. One important result is that the fractal square grid is able to generate

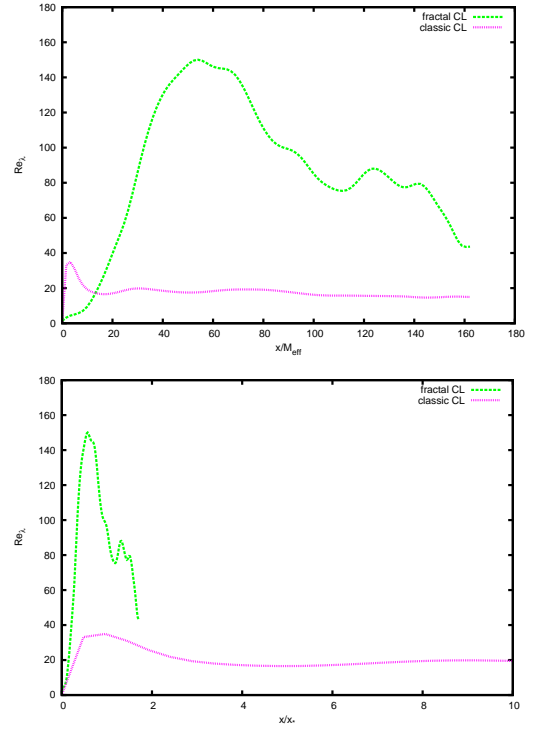


Figure 8. Streamwise evolution of the turbulent Reynolds number based on the Taylor microscale for the two grids on the centreline of the flow.

much higher turbulent intensities than a regular grid for the same Reynolds number  $Re_{M_{eff}}$  and the same blockage ratio, except very close to the grid. For the fractal square grid, we have been able to recover the two different regions already observed in the experiments of [1, 9] for lower blockage ratios: a production region where the flow is non-homogeneous and at the end of which the turbulence peaks followed by a decay region. The main most novel result is that the passive scalar flux is enhanced by an order of magnitude by the fractal square grid.

Further DNS will be required to investigate in more detail the influence of  $S_\theta$ . In particular, it could be interesting to tune  $S_\theta$  with respect to the dissipation so that we can study the passive scalar variance decrease in the streamwise direction. We will then be able to make comparisons with previous works [13, 14] where the properties of a passive scalar field with decaying variance were studied. Another future direction of investigation concerns the influence of the Prandtl number.

#### Acknowledgements

The authors are grateful to Dr. Ning Li for helping with the parallel version of **Incompact3d**. We also thank Eric Lamballais for very useful discussions and acknowledge support from EPSRC Research grants EP/E00847X/1 and EP/F051468/1.

#### REFERENCES

- [1] D. Hurst and J. C. Vassilicos, ‘‘Scalings and decay of fractal-generated turbulence,’’ *Phys. Fluids*, vol. **19**,

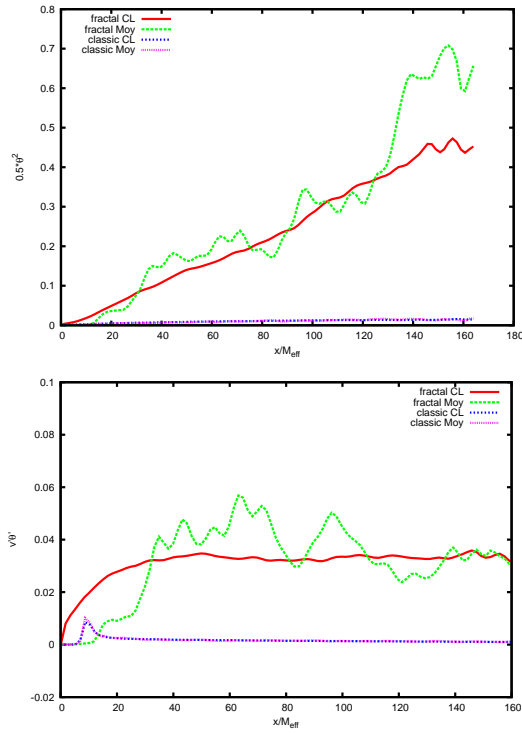


Figure 9. Streamwise evolution of the passive scalar variance (top) and the flux (bottom).

035103, 2007.

- [2] R. E. Seoud and J. C. Vassilicos, "Dissipation and decay of fractal-generated turbulence," *Phys. Fluids*, vol. **19**, 105108, 2007.
- [3] C. Coffey, G. Hunt, R. Seoud, and J. Vassilicos, "Mixing effectiveness of fractal grids for inline static mixers," in *Proof of Concept re-*

*port for the attention of Imperial Innovations.*, (<http://www3.imperial.ac.uk/tmfc/papers/poc>), 2007.

- [4] S. Laizet and E. Lamballais, "High-order compact schemes for incompressible flows: a simple and efficient method with the quasi-spectral accuracy," *J. Comp. Phys.*, vol. **228(16)**, pp. 5989–6015, 2009.
- [5] P. Parnaudeau, J. Carlier, D. Heitz, and E. Lamballais, "Experimental and numerical studies of the flow over a circular cylinder at Reynolds number 3900," *Phys. Fluids*, vol. **20**, 085101, 2008.
- [6] S. Laizet and N. Li, "Incompact3d, a powerful tool to tackle turbulence problems with up to  $(10^5)$  computational cores," *Int. J. Numer. Methods Fluids*, vol. DOI: 10.1002/flid.2480, 2011.
- [7] S. Corrsin, "Heat transfer in isotropic turbulence," *J. Applied Phys.*, vol. **33(1)**, pp. 113–118, 1952.
- [8] Z. Warhaft, "Passive scalars in turbulent flows," *Ann. Rev. Fluid Mech.*, vol. **32**, pp. 203–240, 2000.
- [9] N. Mazellier and J. Vassilicos, "Turbulence without Richardson-Kolmogorov cascade," *Phys. Fluids*, vol. **22**, 075101, 2010.
- [10] S. Laizet and J. C. Vassilicos, "Multiscale generation of turbulence," *J. of Multiscale Modelling*, vol. **1**, pp. 177–196, 2009.
- [11] S. Laizet and J. Vassilicos, "Dns of fractal-generated turbulence," *Flow, Turbulence and Combustion*, In Revision, 2011.
- [12] P. Sullivan, "Dispersion of a line source in grid turbulence," *Phys. Fluids*, vol. **19**, 159, 1976.
- [13] A. Sirivat and Z. Warhaft, "The effect of a passive cross-stream temperature gradient on the evolution of temperature variance and heat flux in grid turbulence," *J. Fluid Mech.*, vol. **128**, pp. 323–346, 1983.
- [14] A. Pumir, "A numerical study of the mixing of a passive scalar in three dimensions in the presence of a mean gradient," *Phys. Fluids*, vol. **6**, 2118, 1994.